

BEST AVAILABLE COPY

IN THE DRAWINGS:

Replacement drawings are submitted for Figures 7 and 8 changing "E_G fluctuation" to "standard deviation of E_G fluctuation".

REMARKS

Initially, applicants would like to thank Examiner Hu for granting an interview and for his time spent at the interview.

Replacement drawing figures are submitted for Figures 7 and 8 that change the horizontal label to "standard deviation of E_g fluctuation (meV)" consistent with page 44, lines 7-10 of the application as filed. Since this description is disclosed in the application as filed, the drawing changes are not believed to present new matter. In addition, such drawing change is believed to address the drawing objection noted in the Official Action.

The specification has been amended to change the brief description of Figure 7 consistent with what is shown in Figure 7 and to address the specification objection noted on page 2, paragraph 2 of the Official Action.

As to the objection noted on page 2, paragraph 3 of the Official Action, applicants have reviewed page 56, lines 4-6 and it appears that such passage is correct. However, applicants note that any confusion as to page 56 may be because there may be two pages 56 in the copy of the specification as filed. Applicants respectfully request that the Examiner review the official copy of the specification as filed to be sure that the copy of record does not contain duplicate pages 56. If an extra page 56 is present, it should be removed.

Claims 71, 75-80 and 121-128 were previously pending in the application. Claims 126-128 are cancelled and new claims 129-131 are added. Therefore, claims 71, 75-80, 121-125, and 129-131 are presented for consideration.

Claim 71 is amended to address the claim objection noted in the Official Action.

Claims 71, 76, 77, 79, 121, 124, 125 and 127 are rejected as anticipated by DOMEN et al. 6,555,403 and claims 75, 78, 80, 122, 123, 126 and 128 are rejected as unpatentable over DOMEN et al. in view of RAZEGHI 6,459,096 and/or applicants' disclosed prior art.

Reconsideration and withdrawal of the rejections are respectfully requested because the reference to DOMEN et al. does not teach or suggest that for which it is offered. Specifically, as set forth at the interview, Figure 16 of the present application does not show that the macroscopic and microscopic fluctuations have any particular correlation to each other. As pointed out at the interview, it is a depiction of the claimed embodiment.

As pointed out at the interview, DOMEN et al. use a micro-photo-luminescent measurement to measure macroscopic fluctuations. Such micro-photo-luminescent measurement is inapplicable to measure microscopic fluctuations. Microscopic fluctuations are measured from the dependency on photo-

luminescence life-time. See page 58, lines 7-14 of the present application.

Applicants assert that DOMEN et al. teach a peak wavelength distribution of macroscopic fluctuation and that such distribution is obtainable from a measurement that corresponds to the illumination mode (I-mode).

On the contrary, microscopic fluctuations as recited in claim 1 and as disclosed in the present invention are measured using the illumination correction mode (I-C mode). As set forth on page 60, line 3 through page 63, line 4 of the present application, a relationship is set forth such that a dispersion degree of thermal carriers may be estimated by varying the measurement temperature so that the microscopic fluctuation, corresponding to the I-C mode measurement may be obtained.

Applicants submit herewith two articles that may be helpful in understanding the present invention and discerning a difference between DOMEN et al. and what is recited in claim 71.

As seen from these articles, there is a difference between the PL wavelength distribution and the PL intensity distribution at I-C mode and I mode against the same specimen and in the same area. Accordingly, the peak wavelength distribution of macroscopic fluctuations of DOMEN et al. is substantially different from the standard deviation of microscopic and macroscopic fluctuations as recited in claim 71.

Applicants note that the articles are not prior art and are submitted only for a better understanding of the context of the claims.

RAZEGHI is only cited for the features of some of the dependent claims and does not teach or suggest the standard deviations of micro fluctuations being not more than 40 meV as recited in independent claim 71. Therefore, each of the claims pending in the application are believed patentable over the proposed combination of references.

Support for new claim 129 can be found on page 57, for example. Support for new claim 130 can be found on page 60, and support for new claim 131 can be found on page 58, line 7 through page 60, line 20. New claims 129-131 depend from claim 71 and further define the invention and are also believed patentable over the cited prior art.

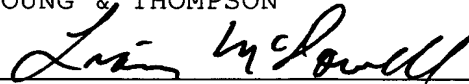
In view of the present amendment and the foregoing remarks, it is believed that the present application has been placed in condition for allowance. Reconsideration and allowance are respectfully requested.

The Commissioner is hereby authorized in this, concurrent, and future replies, to charge payment or credit any

overpayment to Deposit Account No. 25-0120 for any additional
fees required under 37 C.F.R. § 1.16 or under 37 C.F.R. § 1.17.

Respectfully submitted,

YOUNG & THOMPSON

A handwritten signature in cursive script, appearing to read "Liam McDowell", is written over a horizontal line.

Liam McDowell, Reg. No. 44,231
745 South 23rd Street
Arlington, VA 22202
Telephone (703) 521-2297
Telefax (703) 685-0573
(703) 979-4709

LM/lk

APPENDIX:

The Appendix includes the following items:

- Replacement Sheets for Figures 7 and 8 of the drawings
- "Recombination mechanism in low-dimensional nitride semiconductors" article
- "Discrimination of local radiative and nonradiative recombination processes in an InGaN/GaN single-quantum-well structure by a time-resolved multimode scanning near-field optical microscopy" article

Invited Paper

BEST AVAILABLE COPY

Recombination mechanism in low-dimensional nitride semiconductors

Yoichi Kawakami ^{a,*}, Akio Kaneta ^a, Koichi Okamoto ^a, Tsutomu Inoue ^b, Fuminori Satou ^b,
Yoshihito Narita ^b, Fritz Henneberger ^c, Giichi Marutsuki ^d, Yukio Narukawa ^d, Takashi Mukai ^d and
Shigeo Fujita ^a

^a Department of Electronic Science and Engineering, Kyoto University, Kyoto 606-8501, Japan

^b Instruments Development Division, JASCO Corporation, 2967-5, Ishikawa, Hachioji, Tokyo 192-8537, Japan

^c Institut für Physik, Humboldt Universität zu Berlin, Invalidenstr. 110, 10115 Berlin, Germany

^d Nitride Semiconductor Research Laboratory, Nichia Corporation, 491 Oka, Kaminaka, Anan, Tokushima 774-8601, Japan

ABSTRACT

Scanning near field optical microscopy (SNOM) has been developed to assess the recombination mechanism in low-dimensional nitride semiconductors by employing spatial and temporal photoluminescence (PL) mapping under illumination-collection at cryogenic temperatures. The near-field PL images taken at an $\text{In}_x\text{Ga}_{1-x}\text{N}$ single-quantum-well (SQW) structure revealed the variation of both intensity and peak energy according to the probing location with the scale less than a few tens of a nanometer. The PL, the linewidth of which was about 60 meV in macroscopic measurements, was separated into several peaks with the linewidth of about 12 meV if the SNOM-PL was taken with the aperture size of 30 nm. Clear spatial correlation was observed between PL intensity and PL peak-photon-energy, where the regions of strong PL intensity correspond to those of low PL peak-photon-energy. Time-resolved SNOM-PL study showed the important role of exciton/carrier localization in the recombination mechanism in $\text{In}_x\text{Ga}_{1-x}\text{N}$ -based quantum structures.

Keywords: Recombination mechanism, nitride semiconductors, quantum wells, potential fluctuation, scanning near-field optical microscopy, PL mapping, lifetime mapping, exciton localization

1. INTRODUCTION

Recent developments in the growth technology of $\text{In}_x\text{Ga}_{1-x}\text{N}/\text{GaN}/\text{Al}_x\text{Ga}_{1-x}\text{N}$ heterostructures have led to the realization of incandescent violet, blue, green and amber light emitting diodes (LEDs) ^{1,2}, as well as of laser diodes (LDs) ^{3,4} operated from ultraviolet (370nm) to blue (480nm) spectral region. However, there has been in controversy concerning the emission mechanism in $\text{In}_x\text{Ga}_{1-x}\text{N}$ -based semiconductors because of the modulation of optical transitions induced by piezoelectric fields and/or by potential fluctuations as schematically illustrated in Fig.1 ⁵. Such contributions differ between samples due not only to the difference in sample structures, such as mean In mole fraction, film thickness and doping conditions, but also to the difference in growth conditions, such as growth method, gas flow, growth temperatures, and so on. However, it should be noted that the typical well width is as small as 2 to 3 nm for $\text{In}_x\text{Ga}_{1-x}\text{N}/\text{GaN}$ -based light emitting devices in order to avoid the quantum confined Stark effect (QCSE) induced by piezoelectric fields as small as possible because this leads to the separation of wave function between electron and hole resulting in a strong reduction of the oscillator strength for larger well width.

Despite high threading-dislocation density ($10^8 - 10^{10} \text{ cm}^{-2}$) in $\text{In}_x\text{Ga}_{1-x}\text{N}$ -based epilayers grown on sapphire substrates fabricated LEDs show substantially high external quantum efficiency (η_{ext}). The η_{ext} is particularly high in the wavelength from 380 to 490 nm, so that $\eta_{\text{ext}} = \text{about } 20 \%$ is now commercially available, and $\eta_{\text{ext}} = \text{about } 40 \%$ is achieved experimentally in LEDs operated at violet to blue spectral range. Two models have been reported so far to account for such phenomena luminescence dynamics of an InGaN quantum well structure. The first one is that

* Correspondence: Email: kawakami@kuee.kyoto-u.ac.jp; <http://fujita.kuee.kyoto-u.ac.jp>; Telephone: +81-75-753-5295; Fax: +81-753-5898

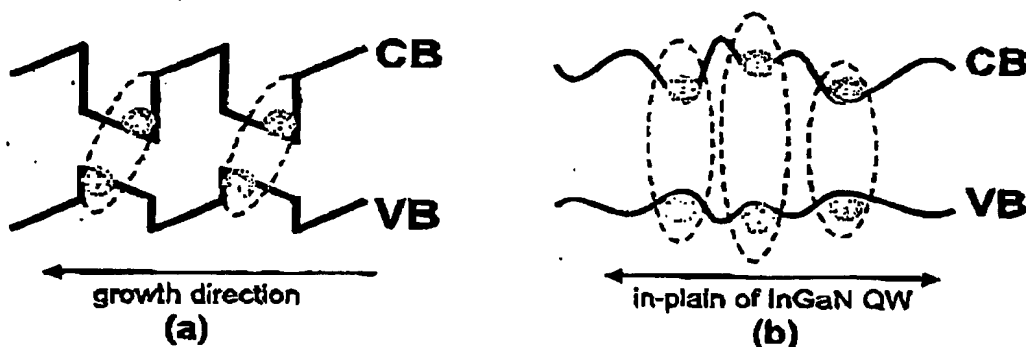


Fig. 1 (a) Piezoelectric field induced in $\text{In}_x\text{Ga}_{1-x}\text{N}/\text{GaN}$ QW grown toward C-axis. (b) Potential fluctuation induced by inhomogeneity of Indium distribution within InGaN QW.

incorporation of In to Ga-site is effective for suppressing nonradiative recombination centers related to point defects.⁷ Another one is the effect of exciton localization induced by compositional fluctuation of In, where the pathways of nonradiative recombination centers are hindered once excitons are captured at potential minima.¹⁰ Nevertheless, it is very important for the further improvement in emission efficiency to correlate radiative/nonradiative recombination processes with micro/nanoscale structures as shown in Fig. 2, and to make a positive-feedback to the design and the fabrication conditions of GaN-based LEDs.

A number of reports have recently been appeared on the spatial mapping of luminescence in $\text{In}_x\text{Ga}_{1-x}\text{N}$ single-quantum-wells (SQWs) by cathodoluminescence (CL),¹⁰⁻¹² or by photoluminescence (PL) using scanning-near field optical microscopy (SNOM).¹³⁻²⁴ Vertikov et al. performed the SNOM-PL mapping in thin $\text{In}_x\text{Ga}_{1-x}\text{N}/\text{GaN}$ epilayers and QWs with the spatial resolution of 100 nm.¹⁴ Figure 3 depicts the three types of configuration used for SNOM-PL measurements. The most of SNOM results were obtained using home-built illumination-mode system, where the laser light was focused into a few hundred nm² spot through the SNOM tip composed of tapered optical fiber and the PL spectra were probed by objective lens. A drawback of such a system is that it is very difficult to know whether excitons and/or carriers producing PL are directly photo-generated at the probe region or they are diffused from outside as can be understood from Fig. 4. The most of SNOM results were obtained using illumination-mode system, which is very difficult to know whether excitons and/or carriers producing PL are directly photo-generated at the probe region or they are diffused from outside. This problem can be overcome by means of illumination-collection mode²⁵ developed recently for the assessment of widegap semiconductors,¹⁸⁻²¹ where photo-excitation and the PL probing are performed using the same fiber tip because the spatial resolution is solely limited by the diameter of aperture formed at the tip of

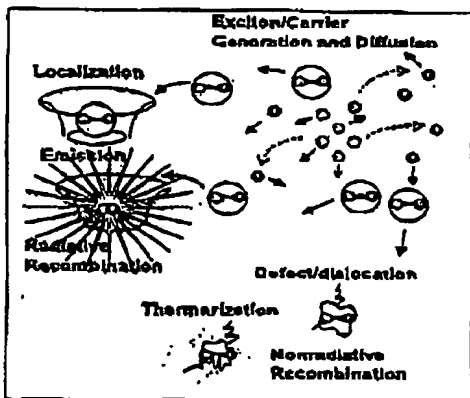


Fig.2 Schematics of radiative and nonradiative recombination dynamics in semiconductors.

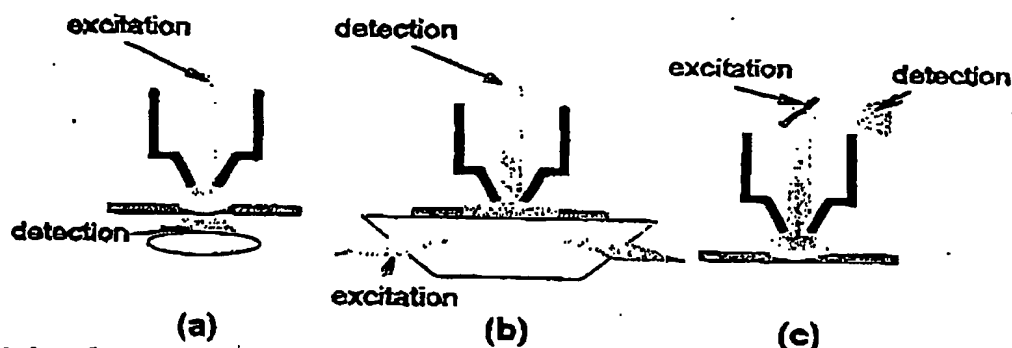


Fig. 3 Optical configuration used for SNOM-PL measurements, (a) illumination mode, (b) collection mode and (c) illumination-collection mode.

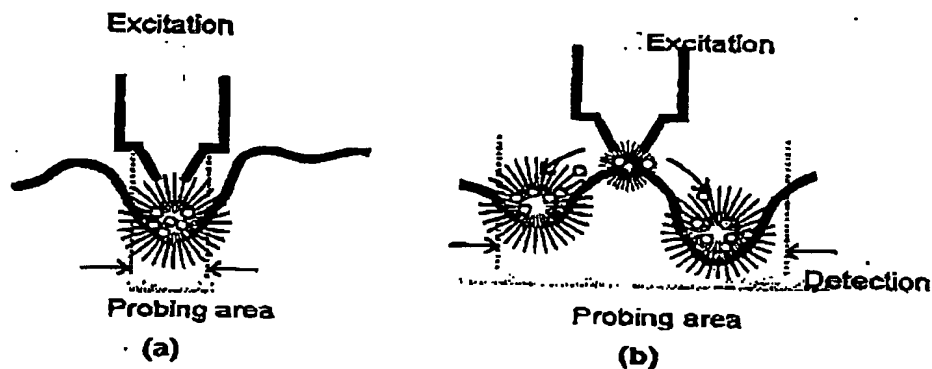


Fig.4 SNOM-PL detection under illumination mode. Spatial resolution is affected as shown in (b) if the photo-generated carriers/excitons diffuse out of the excitation spot before radiative recombination.

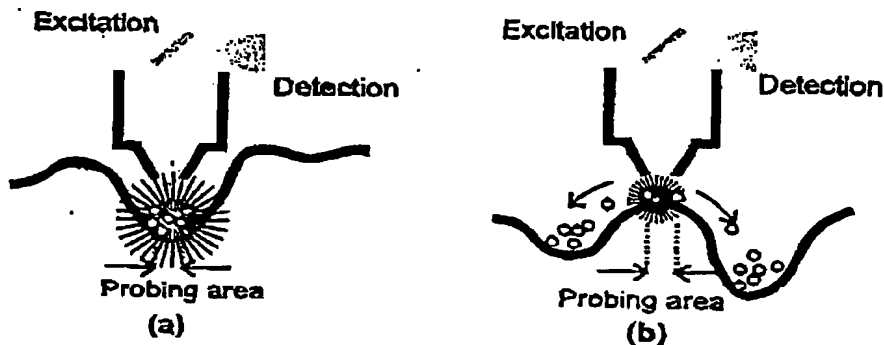


Fig.5 SNOM-PL detection under illumination-collection mode. Spatial resolution is not affected by the carrier/exciton diffusion but limited by the aperture diameter of fiber probe.

fiber probe as shown in Fig. 5.

In this paper, we developed the SNOM technique to characterize the micro/nanoscale optical properties in nitride-based semiconductor. Time-resolved SNOM-PL results taken at an $\text{In}_x\text{Ga}_{1-x}\text{N-SQW}$ structure revealed the critical evidence that supports the model of diffusion of excitons to potential minima.

2. EXPERIMENTAL PROCEDURE

2-1. Instrumentation of SNOM apparatus

The measurements were performed with NFS-300 near-field spectrometer developed at JASCO Corp. that is capable of photoluminescence (PL) mapping with scanning near-field optical microscopy under an illumination collection mode, where both the excitation and the detection are made through the same fibers. In Figs. 6-10, pictures of each part of the apparatus as well as the schematic of the SNOM system are shown.

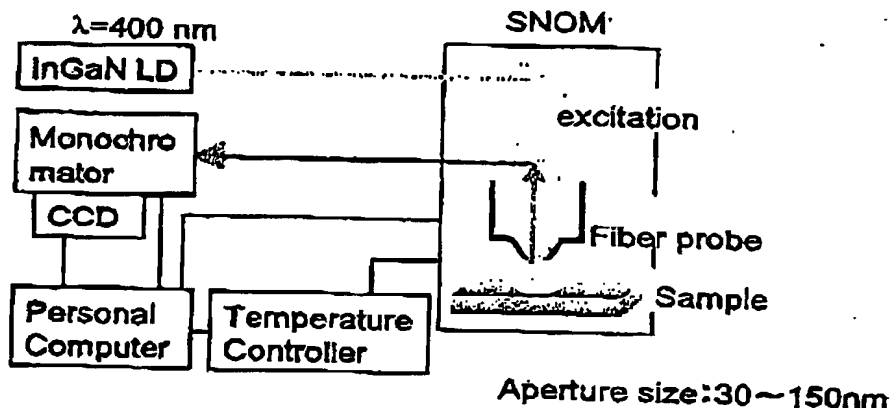


Fig. 6 Schematic of the SNOM system composed of SNOM-head, excitation laser and detection parts.

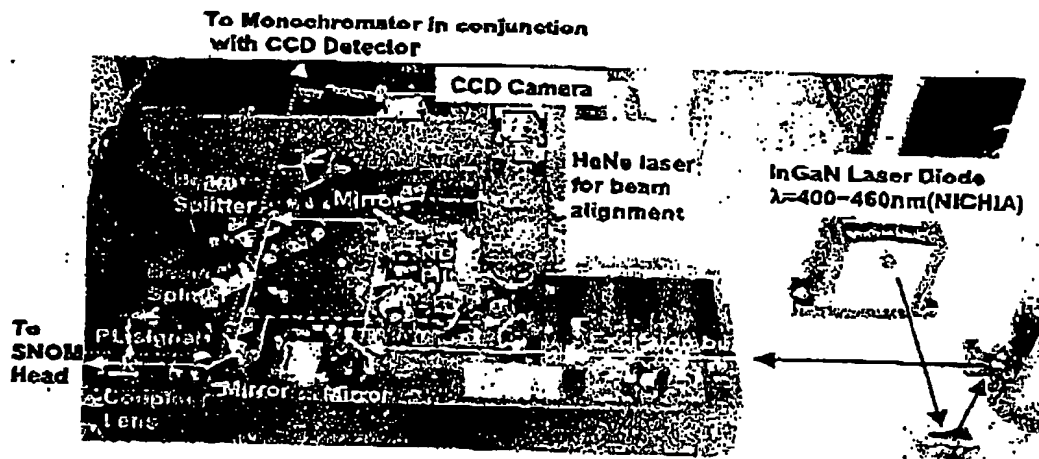


Fig. 7 Excitation and detection optics in the SNOM system.

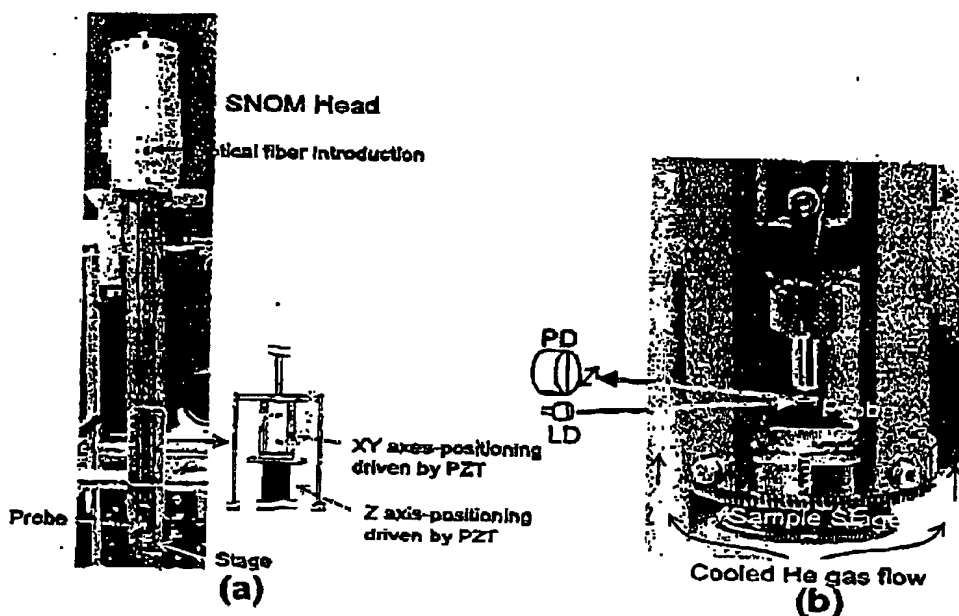


Fig. 8 (a) SNOM-head (whole-view). The position of sample stage is controlled by PZT in xyz directions. (b) The closed view of the sample stage and the probe. The separation between the sample and the fiber tip is controlled by monitoring the friction force using the optical configuration in the figure.

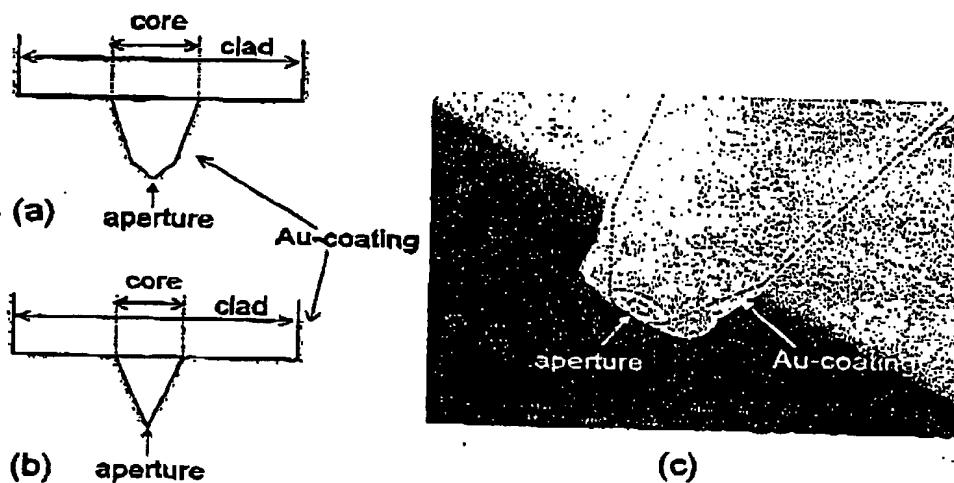


Fig. 9 Schematics of (a) double-tapered Ge-doped-SiO₂ fiber probe, (b) single-tapered pure-SiO₂ fiber probe and (c) SEM picture of the type (a) probe.

Two types of fibers were used in this study; double-tapered Ge-doped-SiO₂ cores with aperture diameter in the range from 30 nm to 150 nm, and single-tapered pure-SiO₂ cores with aperture diameter of 300 nm as shown in Fig. 9. A double tapered structure is fabricated by a multi-step etching technique using hydrofluoric-buffered solution, by which high efficiency of light transmission is achieved compared to that in conventional single-tapered probes²⁶. However, one drawback of this structure is the fluorescence of Ge-doped-SiO₂ core that sometimes buries the PL from the sample in the background level if the signal intensity of PL is not strong enough. Therefore, single-tapered pure-SiO₂ fibers fabricated were used for detecting time-resolved PL, where long exposure-time was enabled by the elimination of fluorescence background. Apertures of fiber probes were obtained by applying the mechanical impact on a suitable surface after evaporating Au at the apex²⁷.

The sample-probe separation was controlled by detecting the amplitude of dithered probe. The amplitude of this oscillation was less than 1 nm at the first-order resonance frequency of the probe. This amplitude was fed back to control the height of the sample PZT (Pb(Zr, Ti)O₃) stage. As a result, the sample-probe separation was regulated to be 10 nm. The cooling of the samples was performed by flowing cool He gas. The stable measurement was achieved by flowing an appropriated flux of He gas from the bottom to the top parts of the cryostat.

An In_{0.4}Ga_{0.6}N-based laser diode emitting at 400 nm (developed at Nichia Corp.) was used as the excitation source. An optical power of 1 mW was coupled to the probe, and about 2 μ W was used to illuminate the samples through the probes of both Ge-doped-SiO₂ fibers with aperture diameter of 100 nm and pure-SiO₂ cores with aperture diameter of 300 nm, while about 0.1 μ W was used through Ge-doped-SiO₂ fibers with aperture diameter of 30 nm. PL signal was collected by the probe, and was introduced into a monochromator in conjunction with a cooled charge-coupled device (CCD) detector (Roper Scientific, Spec-10-400B/LN).

Figure 10 shows the system of time-resolved SNOM-PL measurement. The frequency-doubled mode-locked Al₂O₃:Ti laser emitting at 400 nm with the pulse width of 1.5 ps was used as an excitation source. A streak camera (Hamamatsu Photonics, CS680) was used as a detector. It is noted that the selective photo-excitation to the In_{0.4}Ga_{0.6}N active layer was achieved for both measurements. Since the cut off wavelength of pure-SiO₂ fiber is about 460 nm, the beam propagation properties were assessed by measuring pulse width and spectra before and after passing the fiber of 1m-length. It was found that the broadening of the pulse width after transmission is as small as about 10 ps keeping the same wavelength as shown in Fig. 11. Therefore, the pure-SiO₂ fiber used in this study is capable enough for trying time-resolved SNOM-PL measurement.

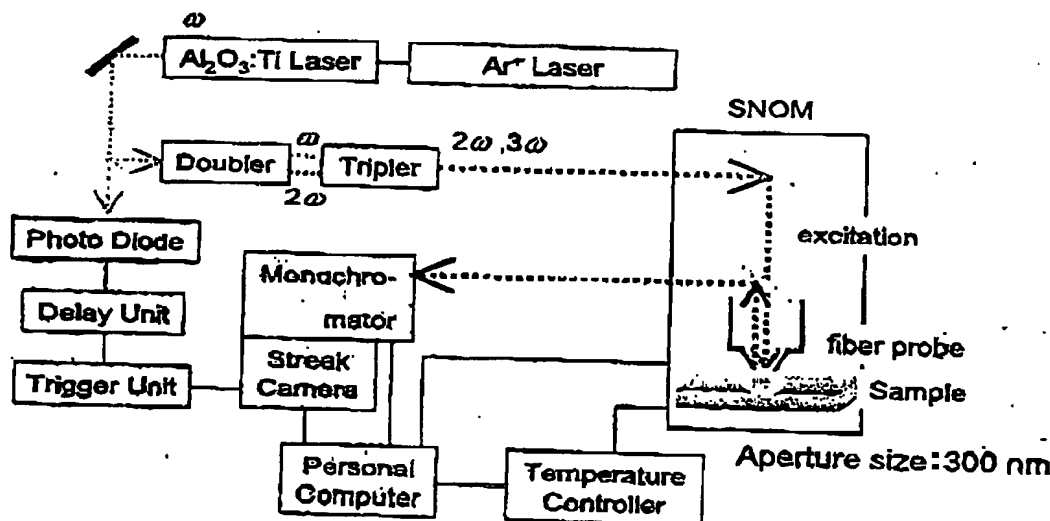


Fig. 10 Schematic of time-resolved SNOM-PL measurement system.

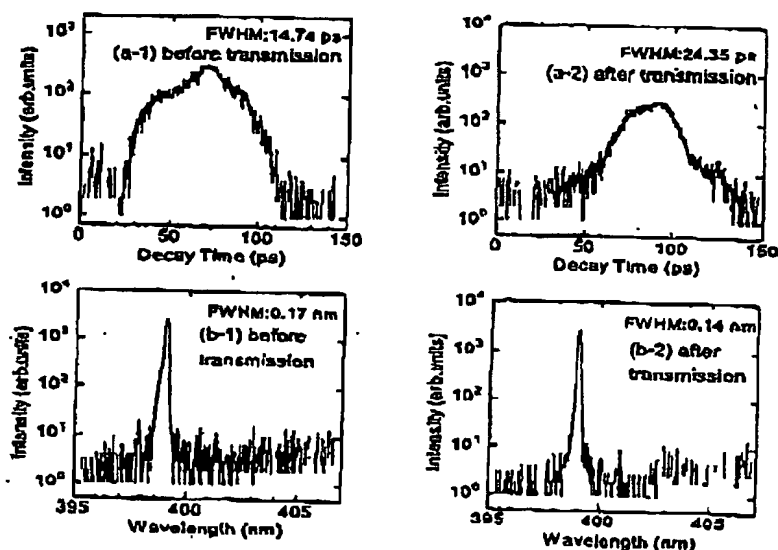
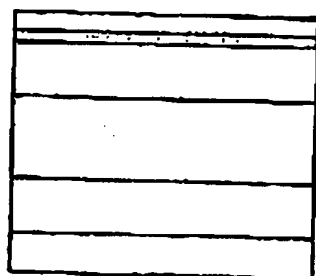


Fig. 11 (a-1, 2) Pulse width of frequency-doubled $\text{Al}_2\text{O}_3:\text{Ti}$ laser measured by the streak camera before and after transmitting pure- SiO_2 fiber. The incident pulse width is 1.5 ps, and the FWHM of 14.74 ps in (a-1) is limited by the measurement resolution. (b-1, 2) the spectra before and after transmitting pure- SiO_2 fiber.

2-2. Sample structure and macroscopic optical properties

The sample (shown in Fig. 12) is grown on sapphire (0002) substrate by metalorganic chemical vapor deposition (MOCVD), and is composed of sapphire (0002) substrate, a 1.5 μm -thick undoped-GaN, a 2.3 μm -thick n-type GaN:Si, a 3nm-thick $\text{In}_{0.2}\text{Ga}_{0.8}\text{N}$ -SQW active layer (x about 0.2) and a 5nm thick undoped GaN layer. Macroscopic PL peak is located at about 480 nm at 20K [Fig. 13 (a)] and at about 490 nm at room temperature. LO-phonon side bands are associated on the low energy-side of the main peak. Temperature dependence of integrated PL-intensity [Fig. 13 (b)] shows that the internal quantum efficiency is nearly unity below 50 K because of the suppression of nonradiative recombination process.



undoped GaN 5 nm
 $\text{In}_{0.2}\text{Ga}_{0.8}\text{N}$ SQW 3 nm
undoped GaN 0.15 μm
Si-doped GaN 2.3 μm
undoped GaN 1.5 μm
 $\text{Al}_2\text{O}_3(0002)$ substrate

Fig. 12 The $\text{In}_{0.2}\text{Ga}_{0.8}\text{N}$ -SQW structure used for the SNOM-measurement.

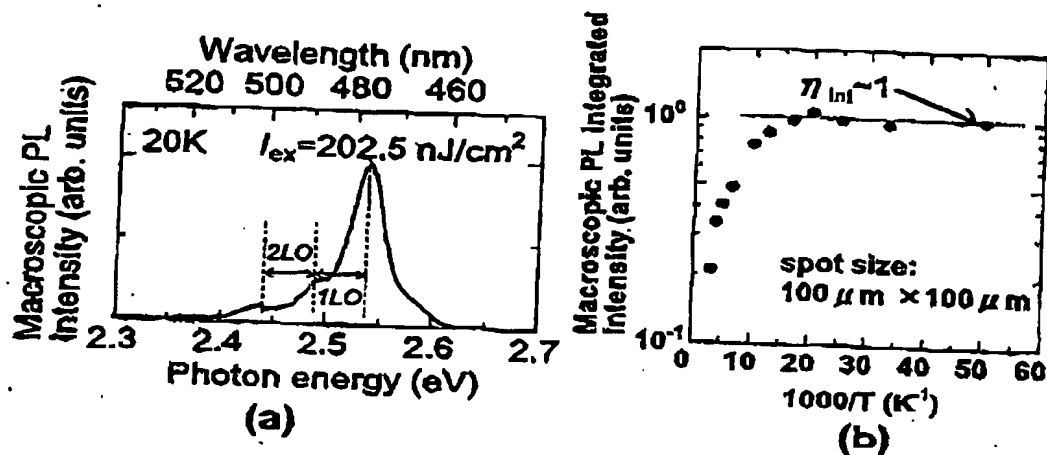


Fig. 13 (a) Macroscopic PL of the sample at 20K taken with the spot size of $100\mu\text{m} \times 100\mu\text{m}$. (b) Macroscopic integrated-PL intensity plotted as a function of inverse of temperature.

RESULTS AND DISCUSSION

Figure 14 shows the PL mapping plotted with PL peak intensity [(a)] as well as with PL peak wavelength [(b)] at 18 K under photo-excitation power density of 100 W/cm^2 . The scanning was made in the area of $4 \times 4 \mu\text{m}^2$ square with an interval of 100 nm using a 150 nm aperture fiber-probe. It was found that the relative PL intensity fluctuates from 1 to 6, and that the PL peak wavelength is distributed from 470 nm to 490 nm, both of which consist of island-like structures within the range approximately 0.1 to $1 \mu\text{m}$.

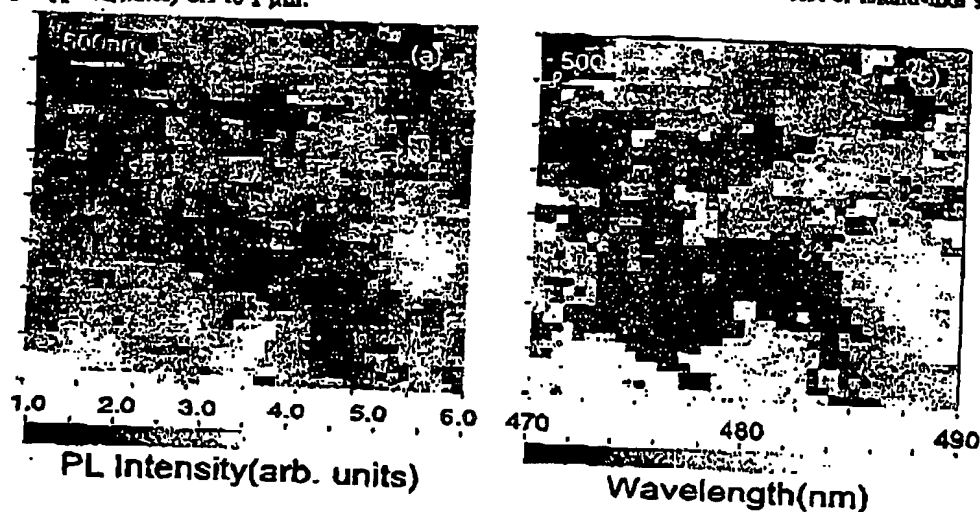


Figure 14 SNOM-PL mapping taken for (a) PL peak intensity and (b) peak wavelength at 18 K.

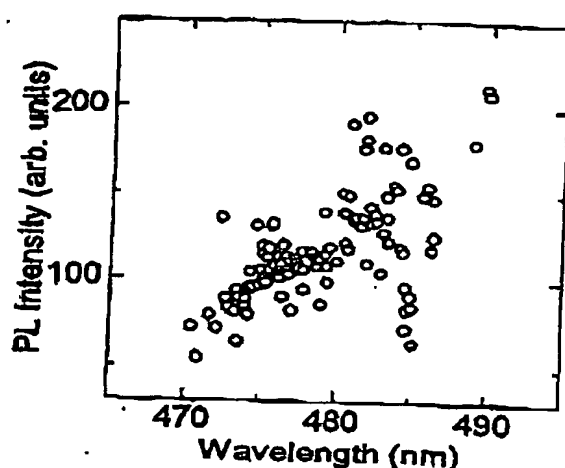
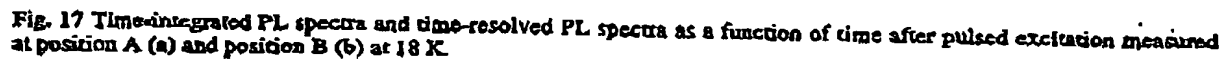
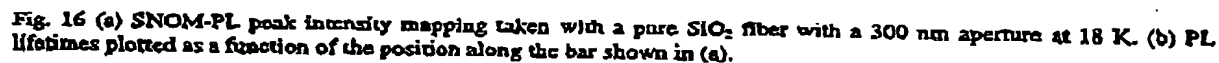


Fig.15 PL peak intensity plotted as a function of PL peak wavelength from the data of SNOM-PL mapping in Fig. 14.

Clear correlation was observed between PL intensity and wavelength as shown Fig. 15, where the areas of strong PL intensity correspond to those of long PL wavelength (low PL peak energy). Temperature dependence of macroscopic PL measurements reveals that the internal quantum efficiency (η_{in}) is nearly unity (0.9-1.0) below 100 K.²² Moreover, atomic force microscopy (AFM) assessed *in-situ* during the SNOM measurements shows that the root mean square of surface unevenness is as small as 5.1 nm within the scanning area of 4 μm^2 square. The PL peak intensity map [figure 1(a)] shows a relative intensity variation of approximately 1 to 6, corresponding to the η_{in} variation of 0.17 to 1.00 if the maximum is 1.00. If nonradiative recombination alone explained the spatial variation, then the spatially averaged quantum efficiency is estimated to be 0.41 taking into account the area of each PL intensity. This value is much smaller than unity that is the macroscopic η_{in} as mention above. Therefore, nonradiative recombination alone cannot explain the results; diffusion of carriers from the low-intensity to the high-intensity regions must occur.

In order to confirm such a mechanism, TRPL was employed under SNOM configuration using a pure SiO_2 fiber-probe with a 300 nm aperture. Figure 16 (a) shows the PL-image mapped with the PL intensity taken under 100 W/cm^2 with continuous wave (CW) condition. TRPL was detected across the white bar drawn in the figure with an interval of 180 nm. The photo excitation energy density is 14 $\mu\text{J}/\text{cm}^2$ in this case. PL lifetimes of the emission peak are plotted as a function of position as shown in Fig. 16 (b). It was found that the short lifetimes (2.5 to 4.8 ns) rapidly jump to the longer ones (7.6 to 9.0 ns) at about 0.75 μm . This position corresponds to the boundary where PL intensity changes from approximately 2.5 to 5.0. The PL lifetime (τ_{PL}) is expressed by the equation by, $1/\tau_{PL} = 1/\tau_{rad} + 1/\tau_{trans} + 1/\tau_{nonrad}$, where τ_{rad} and τ_{nonrad} are radiative and nonradiative lifetimes, respectively, and τ_{trans} represents the transfer lifetime to lower lying energy levels arising from the localization phenomena. As mentioned above, the term of $1/\tau_{trans}$ can be neglected at this temperature. Therefore, the shorter lifetimes at weak PL regions are contributed from the transfer lifetimes. This can be interpreted because PL peak energies of such regions are smaller than other surrounding regions. Figure 17 (a) and (b) show the time-integrated PL, as well as time-resolved PL spectra as a function of time after pulsed-excitation monitored at positions A and B, respectively. Time-integrated PL spectrum in Fig. 17 (a) is composed of two-emission bands peaking at 458 nm and 464 nm. The main PL peak at 458 nm decays with the lifetime of 3.8 ns, while the longer peak at 464 nm does with 6.4 ns. However, for the Fig. 17 (b), the PL-band is composed of single emission peak associated with one LO-phonon replica, and decays with 8.4 ns. Two emission bands with different PL lifetimes in Fig. 17 (a) are probably because the two regions having different energy levels are included within the probing aperture, and the excitons and/or carriers generated at the shorter wavelength region transfer to the longer wavelength regions distributed within or out of the aperture. This model is schematically illustrated in Fig. 18.

SNOM-PL spectra were taken at various excitation power density [(a) 100 W/cm^2 , (b) 1 kW/cm^2 and (c) 10 kW/cm^2] under CW excitation condition as shown in Fig. 19. Each monitored position made the shift toward longer wavelength with increasing excitation power density. However, such shift is not uniformly distributed as revealed from the mapping



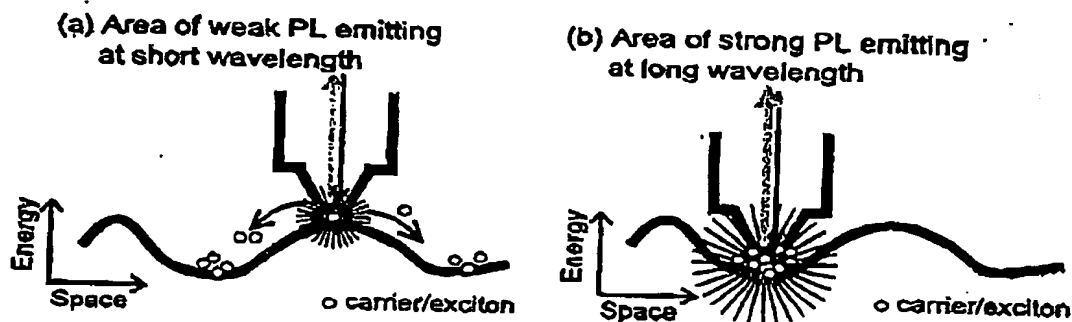


Fig. 18 Model of exciton/carrier localization induced by potential fluctuation, and the correlation with the PL intensity monitored by fiber probe.

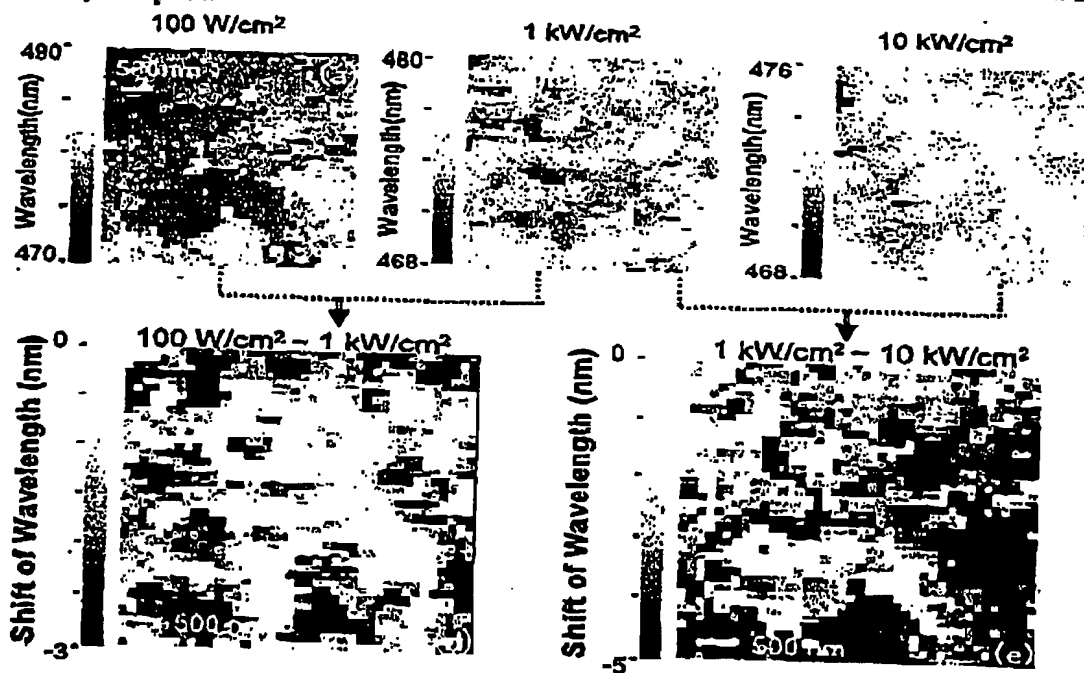


Fig. 19 SNOM-PL mapped with PL peak wavelength under (a) $I_{ex}=100 \text{ W/cm}^2$, (b) 1 kW/cm^2 and (c) 10 kW/cm^2 . Shift of PL peak wavelength between (d) $I_{ex}=100 \text{ W/cm}^2$ and 1 kW/cm^2 , and between (e) $I_{ex}=1 \text{ kW/cm}^2$ and 10 kW/cm^2 .

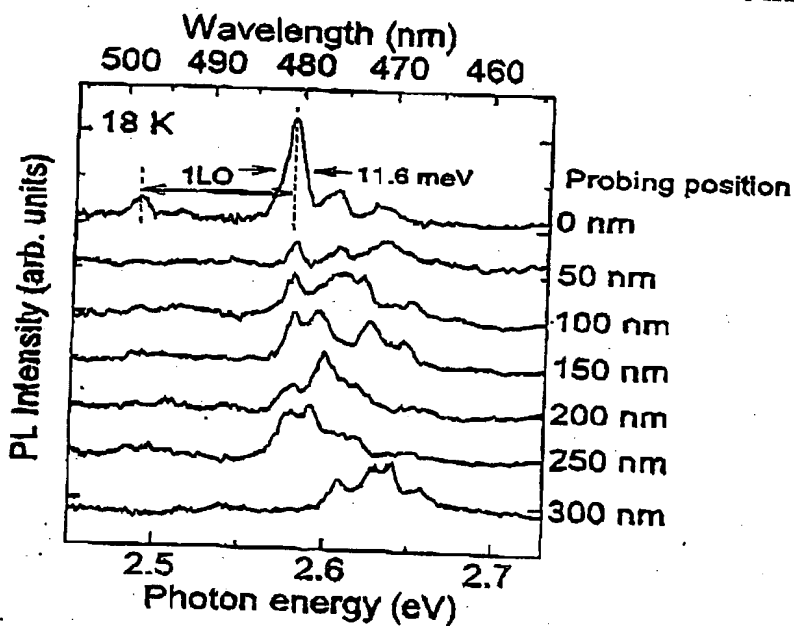
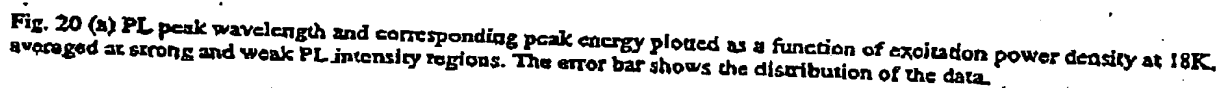


Fig. 21 SNOM-PL spectra taken at each position with a 30nm aperture under $I_{ex}=100 \text{ W/cm}^2$ at 18K.

of wavelength shifts between $I_{ex}=100 \text{ W/cm}^2$ and 1 kW/cm^2 [Fig. 19 (d)], as well as between between $I_{ex}=1.0 \text{ kW/cm}^2$ and 10 kW/cm^2 [Fig. 19 (e)]. Figure 20 shows the PL peak energies plotted as a function of excitation power for two data points, namely for the weak intensity region (averaged 100 data point for smaller value than 25% of PL maximum intensity (I_{max})), and for the strong intensity regions (averaged 100 data point for larger value than 75% of I_{max}). The PL peak energy increases with increasing excitation power in both the strong intensity region and the weak intensity region. However, the blue shift is larger in the weak intensity region than in the strong intensity region for the same excitation intensity. These results can be explained by assuming that the density of states of localized levels decreases with increasing localization depth. Hence, more filling of the exciton and/or carrier band occurs in the weak intensity region than in the strong intensity region for the same excitation intensity. An additional factor that probably contributes to the blue shift in both regions is screening of the quantum well piezoelectric field by the photogenerated excitons and/or carriers.

In order to assess the spatial distribution of localization centers, CW-PL was performed using a 30 nm aperture probe taken at different positions as shown in Fig. 21. Several peaks are clearly observed by using small aperture size fiber-probe and the spectral shape is different from each other. The minimum PL linewidth is about 11.6 meV. This value is one fifth of macroscopic PL linewidth (about 60 meV), indicating that the macroscopic line width is not mainly contributed from the homogeneous broadening due to the interaction with phonon, but from the inhomogeneous one due to potential fluctuation. It is likely that inhomogeneous broadening due to potential fluctuations is still a significant effect on a 30 nm length scale. Therefore, even smaller PL line width might be observed with smaller aperture size.

4. CONCLUSIONS

PL mapping has successfully been performed for an $\text{In}_x\text{Ga}_{1-x}\text{N}$ SQW structure, using SNOM under an illumination collection mode at 18 K. Recombination dynamics was assessed spatially and temporally, indicating the important role of exciton/carrier localization.

ACKNOWLEDGEMENT

Authors would like to thank Drs. Funato and Michelto for valuable comments and discussion. This work was partly supported by the Kyoto University-Venture Business Laboratory Project, the Kawakami Memorial Foundation and by a Grant-in-Aid for the special area research project of Photonics based on wavelength integration and manipulation from the Ministry of Education, Science, Sports and Culture, Japan.

REFERENCES

1. S. Nakamura, M. Senoh, N. Iwasa, S. Nagahama, T. Yamada and T. Mukai, "Superbright green InGaN single-quantum-well-structure light-emitting diodes", *Jpn. J. Appl. Phys.* 34, L1332-L1335, 1995.
2. T. Mukai, H. Narimatsu and S. Nakamura, "Amber InGaN-Based Light-Emitting Diodes Operable at High Ambient Temperatures", *Jpn. J. Appl. Phys.* 37, L479-L481, 1998.
3. T. Mukai, K. Takekawa and S. Nakamura, "InGaN-based blue light-emitting diodes grown on epitaxially laterally overgrown GaN substrates", *Jpn. J. Appl. Phys.* 37, L479-L481, 1998.
4. S. Nagahama, N. Iwasa, M. Senoh, T. Matsushita, Y. Sugimoto, H. Kiyoku, T. Kozaki, M. Sano, H. Matsumura, H. Umemoto, K. Chocho and T. Mukai, "High-power and long-lifetime InGaN multi-quantum-well laser diodes grown on low-dislocation-density GaN substrates", *Jpn. J. Appl. Phys.* 39, L647-L650, 2000.
5. S. Nagahama, T. Yamamoto, M. Sano and T. Mukai, "Ultraviolet GaN Single Quantum Well Laser Diodes", *Jpn. J. Appl. Phys.* 40, L785-L787, 2001.
6. Y. Kawakami, "Chap.10 The optical properties of InGaN-based quantum wells and quantum dots", *Low-Dimensional Nitride Semiconductors*, Oxford Science Publications (edited by B. Gill), 2002.
7. Y. Narukawa, S. Salfou, Y. Kawakami, Sg. Fujita, T. Mukai and S. Nakamura, "Radiative and nonradiative recombination processes in ultraviolet light-emitting diode composed of an $\text{In}_{0.07}\text{Ga}_{0.93}\text{N}$ active layer", *Appl. Phys. Lett.* 74, 558-560, 1999.
8. S. Chiehdhu, T. Azuhara, T. Sota and S. Nakamura, "Spontaneous emission of localized excitons in InGaN single and multi-quantum well structures", *Appl. Phys. Lett.* 69, 4188-4190, 1996.
9. Y. Narukawa, Y. Kawakami, M. Funato, Sz. Fujita, Sg. Fujita and S. Nakamura, "Role of self-formed InGaN quantum dots for exciton localization in the purple laser diode emitting at 420 nm", *Appl. Phys. Lett.* 70, 981-983, 1997.

10. S. Chichibu, K. Wada, and S. Nakamura, "Spatially resolved cathodoluminescence spectra of InGa_N quantum wells", *Appl. Phys. Lett.* 71, 2346-2348, 1997.
11. X. Zhang, D. H. Rich, J. T. Kobayashi, N. P. Kobayashi, and P. D. Dapkus, "Carrier relaxation and recombination in an InGa_N/Ga_N quantum well probed with time-resolved cathodoluminescence", *Appl. Phys. Lett.* 73, 1430-1432, 1998.
12. T. Sugahara, M. Hao, T. Wang, D. Nakagawa, Y. Naoi, K. Nishino, and S. Sakai, "Role of Dislocation in InGa_N Phase Separation", *Jpn. J. Appl. Phys.* 37, L1195-L1198, 1998.
13. P. A. Crowell, D. K. Young, S. Kaller, E. L. Hu, and D. D. Awschalom, "Near-field scanning optical spectroscopy of an InGa_N quantum well", *Appl. Phys. Lett.* 72, 927-929, 1998.
14. A. Verukov, M. Kuball, A. V. Nurmikko, Y. Chen, and S.-Y. Wang, "Near-field optical study of InGa_N/Ga_N epitaxial layers and quantum wells", *Appl. Phys. Lett.* 72, 2645-2647, 1998.
15. A. Verukov, A. V. Nurmikko, K. Doverspike, G. Bulman, and J. Edmond, "Role of localized and extended electronic states in InGa_N/Ga_N quantum wells under high injection, inferred from near-field optical microscopy", *Appl. Phys. Lett.* 73, 493-495, 1998.
16. A. Verukov, I. Ozden, and A. V. Nurmikko, "Investigation of excess carrier diffusion in nitride semiconductors with near-field optical microscopy", *Appl. Phys. Lett.* 74, 850-852, 1999.
17. D. K. Young, M. P. Mack, A. C. Abare, M. Hansen, L. A. Coldren, S. P. Denbaars, E. L. Hu, and D. D. Awschalom, *Appl. Phys. Lett.* 74, "Near-field scanning optical microscopy of indium gallium nitride multiple-quantum-well laser diodes", 2349-2351, 1999.
18. A. Kaneta, T. Izumi, K. Okamoto, Y. Kawakami, Sg. Fujita, Y. Narita, T. Inoue, and T. Mukai, "Spatial Inhomogeneity of Photoluminescence in an InGa_N-Based Light-Emitting Diode Structure Probed by Near-Field optical Microscopy Under Illumination-Collection Mode", *Jpn. J. Appl. Phys.* 40, 110-111, 2001.
19. A. Kaneta, G. Marutsuki, K. Okamoto, Y. Kawakami, Y. Nakagawa, G. Shimomiya, T. Mukai, and Sg. Fujita, "Spatial inhomogeneity of photoluminescence in InGa_N single quantum well structures", *Phys. Status Solidi B* 228, 153-156, 2001.
20. A. Kaneta, K. Okamoto, Y. Kawakami, Sg. Fujita, G. Marutsuki, Y. Narukawa and T. Mukai, "Spatial and temporal luminescence dynamics in an In_xGa_{1-x}N single quantum well probed by near-field optical microscopy", *Appl. Phys. Lett.* 81, 4353-4355, 2002.
21. G. Marutsuki, Y. Narukawa, T. Mitani, T. Mukai, G. Shimomiya, A. Kaneta, Y. Kawakami, Sg. Fujita, "Electroluminescence mapping of InGa_N-based LEDs by SNOM", *Phys. Status Solidi A* 192, 100-116, 2002.
22. M. S. Jeong, Y.-W. Kim, J. O. White, E.-K. Suh, M. G. Cheong, C. S. Kim, C.-H. Hong, and H. J. Lee, "Spatial variation of photoluminescence and related defects in InGa_N/Ga_N quantum wells", *Appl. Phys. Lett.* 79, 3440-3442, 2001.
23. J. Kim, K. Sainice, J. O. White, J.-M. Myoung, and K. Kim, "Near-field photoluminescence spectroscopy of InGa_N films grown by molecular-beam epitaxy", *Appl. Phys. Lett.* 80, 989-991, 2002.
24. J. Kudrna, P. G. Gucciardi, A. Vinattieri, M. Colocci, B. Damilano, F. Semond, N. Grandjean and J. Massies, "Steady-state and time-resolved near-field optical spectroscopy of Ga_N/Al_N quantum dots and InGa_N/Ga_N quantum wells", *Phys. Stat. Sol. (a)* 190, 155-160, 2002.
25. T. Saiki, K. Nishii, and M. Ohtsu, "Low Temperature Near-Field Photoluminescence Spectroscopy of InGaAs Single Quantum Dots", *Jpn. J. Appl. Phys.* 37, 1638-1642, 1998.
26. T. Saiki, S. Mononobe, M. Ohtsu, N. Sato and J. Kusano, "Tailoring a high-transmission fiber probe for photon scanning tunneling microscopy", *Appl. Phys. Lett.* 68, 2612-2614, 1996.
27. T. Saiki and K. Matsuda, "Near-field optical fiber probe optimized for illumination-collection hybrid mode operation", *Appl. Phys. Lett.* 74, 2773-2775, 1999.
28. R. V. Miller, D. A. Kleinman, W. A. Nordland, Jr., and A. C. Gossard, "Luminescence studies of optically pumped quantum wells in GaAs-Al_xGa_{1-x}As multilayer structures", *Phys. Rev. B* 22, 863-871, 1980.
29. K. Okamoto, K. Inoue, Y. Kawakami, Y. Kawakami, M. Terajima, A. Tsujimura and I. Kidoguchi, "Nonradiative recombination processes of carriers in InGa_N/Ga_N probed by the microscopic transient lens spectroscopy", *Rev. Sci. Instrum.* (in press).

16

Appl. Phys. Lett., Vol. 83, No. 17, 27 October 2003

Kanata et al. 3463

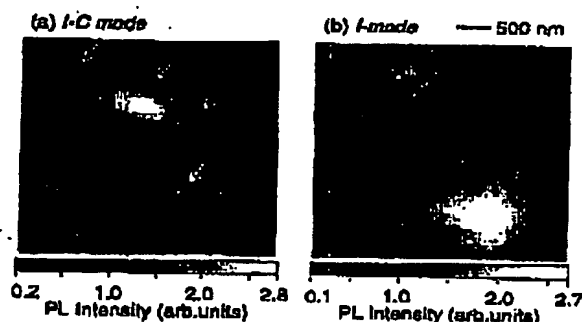


FIG. 2. Near-field PL intensity images taken under I-C mode (a) and I-mode (b) probed with double tapered fiber (aperture size is 200 nm in diameter) at RT. The excitation power density is 2.5 kW/cm² under cw condition. The scanning area is 4 μ m \times 4 μ m with probing step of 100 nm. The PL intensity is normalized to unity.

high resolution and we could clearly discriminate radiative and nonradiative processes in In_xGa_{1-x}N-based semiconductors.

The sample is composed of a sapphire (0002) substrate, a 4- μ m-thick undoped GaN, a 3-nm-thick In_xGa_{1-x}N-SQW active layer (x =about 0.2) and a 5-nm-thick undoped GaN layer. Macroscopic PL peak is located at about 460 nm at RT. A schematic experimental setup is shown in Fig. 1. The measurements were performed with NFS-300 near-field spectrometer developed at JASCO Corp. The tapered structure of fiber probe is fabricated by etching using hydrofluoric-buffered solution.⁹ An In_xGa_{1-x}N-based laser diode emitting at 400 nm (developed at Nichia Corp.) was used as the excitation source of cw PL. The cw PL signal was introduced into a 50-cm monochromator, and then detected by a liquid-nitrogen-cooled CCD detector (Roper Scientific, Spec-10:100B/LN). A frequency-doubled, mode-locked Al₂O₃:Ti laser emitting at 400 nm with the pulse width of 1.5 ps was used as an excitation source. A streak camera (Hamamatsu Photonics, C5680) was used as a detector. The measurements were performed at room temperature.

Figure 2 shows spatial distribution of PL peak intensity under I-C mode (a) and I-mode (b) taken in the same scanning area. Concerning the I-C mode measurement, it was found that relative PL intensity fluctuates from 0.2 to 2.8, consisting of island like structures within the range of approximately 0.3–1 μ m. On the other hand, in I-mode measurement, relative PL intensity fluctuates from 0.1 to 2.7, a

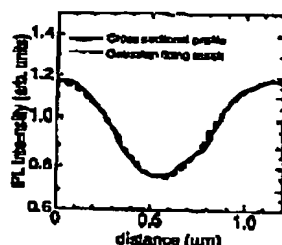


FIG. 3. Cross-sectional profile of PL intensity along the white bar in Fig. 2(a).

Downloaded 13 Aug 2004 to 128.174.211.53. Redistribution subject to AIP license or copyright; see <http://apl.aip.org/apl/copyright.jsp>

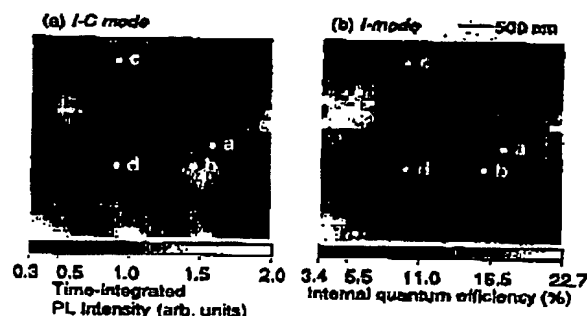


FIG. 4. Time-integrated near-field PL intensity images taken under I-C mode (a) and I-mode (b) probed with single tapered fiber (pure SiO₂, aperture size is 200 nm in diameter) at RT. The excitation power density is 5.5 μ W/cm² under pulsed condition. The scanning area is 3.7 μ m \times 3.7 μ m with the probing step of 100 nm. The PL intensity is normalized to unity.

value larger than that of I-C mode. Our SNOM apparatus regulates the sample-probe separation with a shear force (SF) system,¹⁰ SF signal assessed *in situ* during the SNOM measurements shows that the root mean square of surface-roughness is as small as 3.1 nm, and that there is no correlation with PL intensity signal within the scanning area of 4 μ m \times 4 μ m. In Figs. 2(a) and 2(b), we show the I-C mode and I-mode maps obtained simultaneously on a certain area of our sample. The two images present quite interesting differences. We can notice the presence of weak PL intensity domains in I-C mode (indicated by the arrows) that appear as high PL intensity in I-mode. Other regions appear to remain unchanged if observed in the two modes. This behavior can be explained as follows. In the case of domains that appear of weak PL intensity in I-C mode and turn out as high PL intensity in I-mode, we believe that the carrier and/or exciton that are photogenerated directly under the optical aperture of the probe, are diffused and localized to out of the I-C mode probing area, but they remain in the range of the far-field I-mode detector.

In the other case, the photogenerated carriers and/or excitons do not migrate further than the I-C mode probing region, they are presumably captured at nonradiative recombination centers, origin of which are related to microscopic dislocations and/or to nanoscopic point defects. A cross-sectional profile of PL intensity along the white line in Fig. 2(a) is plotted in Fig. 3. The full width at half-maximum of a Gaussian fitting result of this profile is 550 nm; therefore, the diffusion length to radiative recombination center is at least

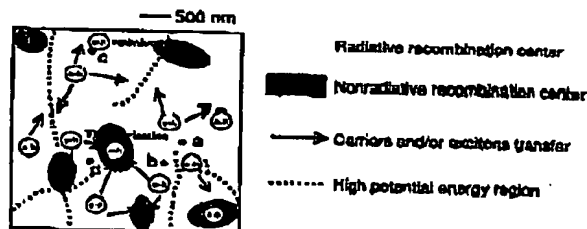


FIG. 5. Schematics of the different carrier dynamics as observed in Fig. 4 with its four studied points a, b, c, and d.

TABLE I. We classified the carrier dynamics observation of Fig. 4 in four different behavior classes, each represented by the four points (a,b,c, and d) in this table.

Position	I-C mode	I-mode	η_{int} (%)	$\tau_{\text{PL-I-C}}$ (ns)	$\tau_{\text{PL-I}}$ (ns)	τ_{trans} (ns)	τ_{rad} (ns)	τ_{nonrad} (ns)
a	Weak	Strong	21.1	0.341	1.553	0.83	7.35	1.97
b	Strong	Weak	15.0	0.580	0.673	4.18	4.49	0.79
c	Strong	Strong	22.6	0.564	0.568	87.1	2.50	0.73
d	Weak	Weak	9.0	0.552	0.677	3.00	7.44	0.74

275 nm in this area. It is interesting to note that the similar value is reported by Cherns *et al.* as the diffusion length in InGaN-based quantum structures using cathodoluminescence spectroscopy technique.¹¹

Figures 4(a) and 4(b) show the time-integrated PL intensity mapped in I-C mode and I-mode, respectively. TRPL was detected at four different positions that are indicated with the letters (a)-(d). These positions were selected as representative of four different behaviors: (a) relatively weak PL intensity in I-C mode while stronger PL intensity in I-mode; (b) opposite situation to the case of (a); (c) relatively strong PL intensity in both modes; and (d) relatively weak PL intensity in both modes. It was found that the PL lifetimes (τ_{PL}) under I-C mode are always shorter than those in I-mode. The difference is significant for the data at (a), where τ_{PL} values are 0.341 and 1.553 ns, for I-C mode and I-mode, respectively. The PL lifetime in I-C mode ($\tau_{\text{PL-I-C}}$) is $1/\tau_{\text{PL-I-C}} = 1/\tau_{\text{rad}} + 1/\tau_{\text{nonrad}} + 1/\tau_{\text{trans}}$, where τ_{rad} and τ_{nonrad} are radiative and nonradiative lifetimes, respectively, and τ_{trans} represents the lifetime of carrier transfer from the area directly under the tip aperture (within the I-C mode probing range, I-C mode and I-mode detection are both possible) and a region external to it (in this case, only I-mode detection is possible). Since a PL signal is detected in far-field configuration under I-mode, the term of $1/\tau_{\text{trans}}$ can be neglected; the PL lifetime under I-mode ($\tau_{\text{PL-I}}$) is expressed by $1/\tau_{\text{PL-I}} = 1/\tau_{\text{rad}} + 1/\tau_{\text{nonrad}}$. PL intensity mapped under I-mode [Fig. 4(b)] represent the spatial distribution of internal quantum efficiency. According to the temperature dependence of macroscopic PL measurements, it was found that the internal quantum efficiency of this sample is nearly unity (more than 90%) at temperatures less than 50 K.¹² Consequently, the distribution of PL intensities from 0.1 to 2.7 at RT corresponds to η_{int} values ranging from 3.4% to 22.7%. Since the η_{int} value is expressed by $\eta_{\text{int}} = \tau_{\text{nonrad}}/(\tau_{\text{rad}} + \tau_{\text{nonrad}})$, all recombination lifetimes can be calculated using the experimental data as shown in Table I.¹³ It is evident that the shorter lifetime of $\tau_{\text{PL-I-C}}$ probed at position (a) is due to a small $\tau_{\text{trans}} = 0.83$ ns-term. This transfer process is probably caused by exciton/carrier localization centers that are local potential minima distributed in the proximity of the tip, but external of the I-C mode probing range. This idea is confirmed by examining the time integration of the PL peaks, in the case of position (a) the time integrated peak is located at 461.9 nm (2.683 eV) under I-C mode, while it is at 464.2 nm (2.670 eV) under I-mode.

In the point indicated with (b), relatively weak PL intensity in I-mode is caused by a transfer process to nonradiative recombination centers distributed in the region external to the I-C mode probing, as it is indicated by the small $\tau_{\text{trans}} = 0.79$ ns. Concerning the point in (c), the strong PL inten-

sities in both modes are due to radiative recombinations that mainly take place within the aperture, as shown by a large value of $\tau_{\text{trans}} = 87.1$ ns. Moreover, in the position (d), a weak PL intensity in both modes is due by large density of nonradiative recombination centers distributed within and outside of the aperture range.

Based on the dynamics just described, the transfer, radiative, and nonradiative processes taking place are represented in the scheme of Fig. 5. Radiative and nonradiative recombination centers are present all over the sample. However, their densities is inhomogeneous. Higher density of radiative recombination domains act as attractive centers for photogenerated excitons/carriers. Potential energy was estimated by the mapping of PL peak; in Fig. 5, the dotted lines represent regions where the potential energy is higher. These high-energy lines form a potential ridge that presumably would suppress the carrier/exciton diffusion, creating the carrier dynamic we observed.

The authors would like to thank Dr. Funato and Dr. Micheletto for valuable comments and discussion. We are also grateful to Mr. Narita at JASCO Corp. for contributing the setup of SNOM. This work was partly supported by the Kyoto University-Venture Business Laboratory Project, the Mizuho Foundation for the Promotion of Sciences, the 21st Century COE Program (No. 14213201), and by a Grant-in-Aid for the special area research project of Photonics based on wavelength integration and manipulation from the Ministry of Education, Science, Sports and Culture, Japan.

- S. Nakamura, M. Senoh, N. Iwasa, and S. Nagahama, *Jpn. J. Appl. Phys.* **34**, L797 (1995).
- S. Nakamura, M. Senoh, N. Iwasa, S. Nagahama, T. Yamada, and T. Mukai, *Jpn. J. Appl. Phys.* **34**, L1332 (1995).
- T. Mukai, H. Narimatsu, and S. Nakamura, *Jpn. J. Appl. Phys.* **37**, L479 (1998).
- M. Yamada, Y. Narukawa, and T. Mukai, *Jpn. J. Appl. Phys.* **41**, L246 (2002).
- Y. Narukawa, S. Saitou, Y. Kawakami, S. Fujita, T. Mukai, and S. Nakamura, *Appl. Phys. Lett.* **74**, 558 (1999).
- S. Chichibu, T. Azuhata, T. Sota, and S. Nakamura, *Appl. Phys. Lett.* **69**, 4188 (1996).
- Y. Narukawa, Y. Kawakami, M. Funato, S. Fujita, S. Fujita, and S. Nakamura, *Appl. Phys. Lett.* **70**, 981 (1997).
- A. Kaneta, K. Okamoto, Y. Kawakami, S. Fujita, G. Maruishi, Y. Narukawa, and T. Mukai, *Appl. Phys. Lett.* **81**, 4353 (2002).
- T. Sakai, K. Nishi, and M. Ohno, *Jpn. J. Appl. Phys.* **37**, 1638 (1998).
- E. Bezig, P. L. Finn, and J. S. Weiner, *Appl. Phys. Lett.* **60**, 2484 (1992).
- D. Cherns, S. J. Henley, and P. A. Ponce, *Appl. Phys. Lett.* **78**, 2691 (2001).
- R. C. Miller, D. A. Kleinman, W. A. Nordland, Jr., and A. C. Gosard, *Phys. Rev. B* **22**, 863 (1980).
- The first-order assumption used in this calculation, where radiative lifetimes as well as nonradiative lifetimes in illumination mode are same as those in illumination collection mode. More detailed analysis taking into account the difference in radiative/nonradiative lifetimes are in progress.

**This Page is Inserted by IFW Indexing and Scanning
Operations and is not part of the Official Record**

BEST AVAILABLE IMAGES

Defective images within this document are accurate representations of the original documents submitted by the applicant.

Defects in the images include but are not limited to the items checked:

- ☐ **BLACK BORDERS**
- ☐ **IMAGE CUT OFF AT TOP, BOTTOM OR SIDES**
- ☐ **FADED TEXT OR DRAWING**
- ☐ **BLURRED OR ILLEGIBLE TEXT OR DRAWING**
- ☐ **SKEWED/SLANTED IMAGES**
- ☐ **COLOR OR BLACK AND WHITE PHOTOGRAPHS**
- ☐ **GRAY SCALE DOCUMENTS**
- ☐ **LINES OR MARKS ON ORIGINAL DOCUMENT**
- ☐ **REFERENCE(S) OR EXHIBIT(S) SUBMITTED ARE POOR QUALITY**
- ☐ **OTHER:** _____

IMAGES ARE BEST AVAILABLE COPY.

As rescanning these documents will not correct the image problems checked, please do not report these problems to the IFW Image Problem Mailbox.